Plasma Chemistry and Plasma Processing (2023) 43:2065–2078
https://doi.org/10.1007/s11090-023-10343-w

ORIGINAL PAPER

Non-Oxidative Ethane Dehydrogenation in a Packed-Bed DBD Plasma Reactor

Fabio Cameli[1,2] · Panagiotis Dimitrakellis[1,3] · Georgios D. Stefanidis[2,4] · Dionisios G. Vlachos[1,3]

Received: 22 April 2023 / Accepted: 29 May 2023 / Published online: 15 June 2023

Abstract
Plasma-assisted conversion of ethane (C_2H_6) can produce value-added chemical building blocks using green electricity. Here we employ a simple packed-bed coaxial dielectric barrier discharge (DBD) reactor to convert C_2H_6 at mild operating conditions unattainable by conventional thermocatalysis. Ethylene (C_2H_4), acetylene (C_2H_2), and methane (CH_4) are the main products along with small fractions of C_3 and C_4 hydrocarbons. Interestingly, the C_2H_4 selectivity is primarily correlated to C_2H_6 conversion, dominated by electron dissociation and recombination reactions irrespective of the dielectric properties of the packed bed material (SiO_2, Al_2O_3, ZrO_2, TiO_2, and $BaTiO_3$), packing material size, supplied power, and C_2H_6 concentration. While a distortion of the electric field and discharge propagation results in varying dissipated power as materials change, the C_2H_4 energy yield remains constant. The particle size appears to affect conversion mainly due to pressure alterations. Pd/SiO_2 catalyst can change the selectivity, favoring saturated species by expending hydrogen.

Keywords Ethane dehydrogenation · Non-thermal plasma · Dielectric barrier discharge · Ethylene

✉ Dionisios G. Vlachos
vlachos@udel.edu

[1] Department of Chemical and Biomolecular Engineering, University of Delaware, 150 Academy St, Newark, DE 19716, USA

[2] Laboratory for Chemical Technology, Ghent University, Gent, Belgium

[3] Catalysis Center for Energy Innovation, Delaware Energy Institute (DEI), RAPID Manufacturing Institute, 221 Academy St, Newark, DE 19716, USA

[4] School of Chemical Engineering, National Technical University of Athens, Athens, Greece

Introduction

The intensive shale gas exploitation has drastically reshaped the energy and chemicals market. Whilst methane (CH_4) is its most abundant component, ethane (C_2H_6) amounts to about 10% and can be transformed into value-added products, such as ethylene (C_2H_4) and acetylene (C_2H_2) [1]. The established naphtha cracking for C_2H_4 (and propylene, C_3H_6) production has lately been challenged by C_2H_6 (and propane, C_3H_8) dehydrogenation due to abundance and low cost of shale gas [2]. The state-of-the-art C_2H_6 dehydrogenation relies on thermocatalytic conversion requiring high temperatures (i.e., 550 to 700 °C to attain conversion up to 40%) and a considerable energy input, having low energy efficiency in the heat exchanger and producing copious emissions of CO_2 [3–5]. The difficult activation of the C-H bond, the catalyst deactivation and cost, e.g., Pt-based, or toxicity, e.g., CrOx-based, and the equilibrium limitations are additional challenges of this process. In this context, a highly reactive non-thermal plasma could convert C_2H_6 at low temperatures with lower energy. Moreover, the operation of a plasma reactor by electrical (including intermittent) energy allows for deployment in remote areas typical of extraction sites [6, 7].

Several plasma reactors have been showcased for non-oxidative coupling [8] and dry reforming [9] of CH_4. Dielectric barrier discharges (DBD) are ideal for studying plasma-catalyst interactions, [10, 11] whereas spark discharges promote higher gas temperature and attain higher energy efficiency [12]. Contrariwise, limited literature has been devoted to C_2H_6, [13–15] focusing mainly on oxidative dehydrogenation (ODH) with CO_2 as a soft oxidant [16–18]. The main products of ODH include C_2H_4, C_2H_2, and CH_4, whereas C-C coupling reactions into higher hydrocarbon chains have also been observed. Syngas is also produced via this route. In a recent work on ODH, several oxygenated species were produced with selectivity below 4% [18]. All the ODH works report C_2H_4 yield of about 2-3.5% [17, 18] with the highest value of 14% attained with a Pd catalyst [16]. The only examples of non-oxidative C_2H_6 dehydrogenation (EDH) include a plasma jet that favors CH_4 production over C_2H_4 [15] and a low-pressure plasma reactor promoting C_2H_2 and CH_4 over C_2H_4 [13].

Here, we explore plasma-assisted non-oxidative conversion of C_2H_6 into olefins and light hydrocarbons at atmospheric pressure. A packed-bed coaxial DBD reactor is employed to test packing materials of different dielectric properties and particle size while controlling the dissipated power and residence time. Finally, a silica supported Pd catalyst is compared to bare silica to underscore the catalytic effect on product selectivity and the dielectric effect on C_2H_6 conversion.

Experimental

Figure 1 shows a schematic of the experimental set-up, a close-up of the DBD reactor, and a picture with ignited plasma. The coaxial DBD plasma reactor comprises a quartz tube (9.6 mm outer diameter, 6.8 mm inner diameter) around which a copper foil (13 mm long) is wrapped serving as the high voltage electrode. A stainless-steel rod (diameter 3 mm) is placed in the center of the tube and is connected to the circuit ground. The packing bed occupies the tube between the electrodes, while a layer of glass wool (4 μm, Technical Glass Products) is placed before the bed. The feed gas comprises C_2H_6 (purity > 99.995%, Mathe-

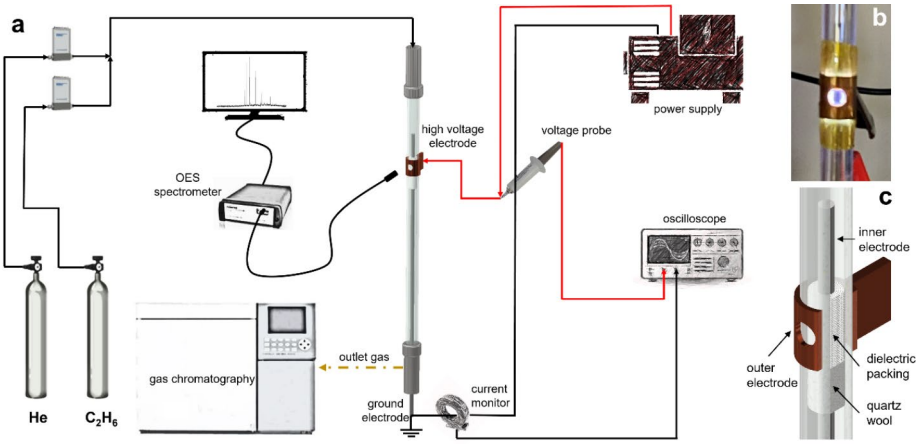

Fig. 1 (a) Schematic of the DBD packed-bed plasma reactor set-up with auxiliary units: He/C_2H_6 gas feed, sinusoidal power generator, OES spectrometer, gas chromatograph, electrical waveforms acquisition through oscilloscope, and voltage and current probe. (b) Real image of plasma inside the DBD reactor without packing. (c) Section of the packed reactor with dielectric packing in the plasma region laying on a layer of quartz wool.

son) and Helium (He, 99.999%, Keen Gas) with flow rates (3–12 sccm for C_2H_6 and 57–228 sccm for He) regulated via mass flow controllers (GF40 series, Brooks). C_2H_6 dilution in He is necessary to facilitate plasma ignition and sustainment. In an industrial setting, He could be replaced by Argon to improve plant's economics. The gas outlet is routed to a gas chromatograph (GC) (Agilent Plot/Q). A sinusoidal high voltage (6–10 kV peak-to-peak) is supplied to the system (PVM500) through the high voltage electrode. A high voltage probe (Tektronix P6015A) and a current monitor (Pearson 2100) are used for monitoring the voltage – current signals via an oscilloscope (Tektronix MDO34). The dissipated power P (W) is calculated from the voltage u (V) and current i (A) waveforms via Eq. (1):

$$P = \frac{1}{T}\int u\,(t) \times i\,(t)\,dt \tag{1}$$

The yield (Y) and product-based selectivity (S) of each product (i) are calculated using Eqs. (2) and (3), respectively:

$$Y_i\,(\%) = \frac{\nu_i \cdot C_i}{2 \cdot {C_2H_6}^{in}} \times 100\,(\%) \tag{2}$$

$$S_i\,(\%) = \frac{\nu_i \cdot C_i}{\sum \nu_i \cdot C_i} \times 100\,(\%) \tag{3}$$

where ν_i is the number of carbon atoms, C_i is its outlet gas concentration, and ${C_2H_6}^{in}$ is the C_2H_6 inlet concentration.

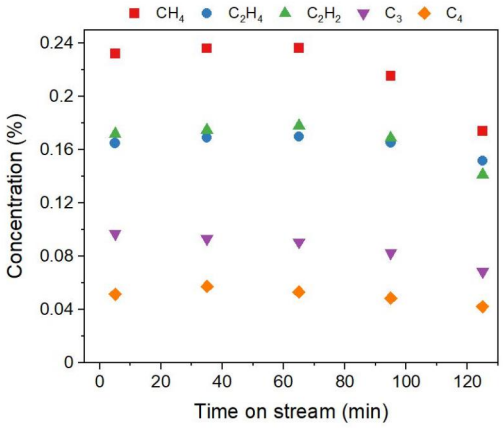

Fig. 2 Product fractions vs. time on stream for a SiO_2 packed-bed plasma reactor. Flow rate: 60 sccm (5% C_2H_6 in He). Peak-to-peak voltage: 12 kV. Particle size: 250–425 µm

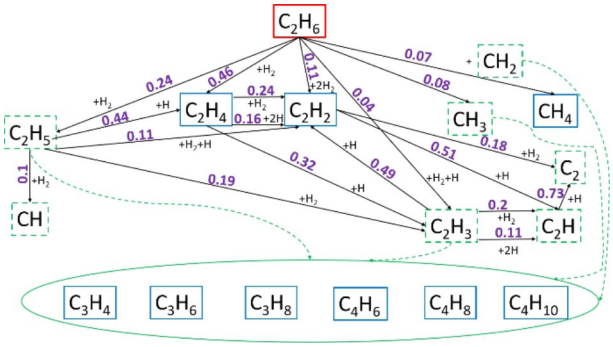

Fig. 3 Proposed reaction network of identified species (blue solid line boxes) through main electron impact dissociation and radical recombination reactions (green dashed line boxes). Branching ratios for each dissociation route in purple taken from Ref. [19]

The packing materials (i.e., SiO_2, Al_2O_3, ZrO_2, TiO_2, and $BaTiO_3$) were purchased in nanopowder form (US Research Nanomaterials, Inc.), calcined (400 °C for 4 h), pelletized, and sieved (particle size distribution 145–560 µm). The materials filled up the interelectrode zone (details in ESI). The Pd/SiO_2 catalyst was prepared by incipient wetness impregnation. A solution of Na_2PdCl_4 (Sigma Aldrich, >99.99%) and distilled water was used for impregnation on SiO_2. The catalyst was dried overnight at 110 °C before calcination. Catalyst reduction was performed directly in the packed bed through a H_2 plasma (10 vol% H_2 in He) for 1 h at 10 kV.

Results

Figure 2 shows the effluent concentrations of all detected products for a packed bed comprising 150 mg of SiO_2 (particle size 250–425 µm) at an applied voltage of 12 kV, a total flow rate of 60 sccm, with 5% C_2H_6 in He. The products are mostly CH_4, C_2H_4, and C_2H_2, and longer isomeric saturated and unsaturated hydrocarbons up to C_4 (Fig. 2; the C_3 and C_4 account for all the saturated and unsaturated species, i.e., 4 species for C_3 and 9 species for C_4). The concentrations are nearly constant at short times and drop at longer time on stream

(i.e., above 90 min) due to a decrease in the conversion likely caused by solid deposit, affecting the plasma. The yellow solid deposit observed mainly on the reactor wall and inner electrode surface and to a lower extent on the particles surface could be ascribed to polymerization of C_2 species. A dedicated study presented this phenomenon in plasma-driven polymerization of C_2H_6 [13]. Hereafter all data reported correspond to 15 min time on stream where the operation is stable and carbon deposit is limited (carbon balance reported in Table S1).

Electron-impact dissociation reactions that form radical species are central in hydrocarbon plasma chemistry [20]. The plasma-induced alkyl and H radicals interact with each other via secondary reactions (neutral-neutral), resulting in a wide range of hydrocarbons with varying carbon number and saturation level. Figure 3 presents the network of electron-impact dissociation reactions leading to the main products reported in Fig. 2. C_2H_6 dissociation mainly results in C_2H_4, C_2H_5, C_2H_2, and CH_4 according to the branching ratio of each dissociation reaction, defined as the contribution of a reaction pathway to the overall cross section of the dissociation processes [19]. C_2H_4 formation is favored over C_2H_2 owing to the lower threshold energy of the electron-impact dissociative excitation of C_2H_6 (i.e., 4 and 6.2 eV for C_2H_4 and C_2H_2, respectively) [19]. Nevertheless, C_2H_2 is also formed via dissociation of C_2H_4 and C_2H_3 that in turn forms from C_2H_4 and C_2H_5. C_2H_2 is subject to electron-impact dissociation like any other species. Ethyl radical (C_2H_5) undergoes electron-impact dissociation to produce chiefly C_2H_4 and to a less extent C_2H_2 and CH.

Packing materials of varying dielectric properties are expected to modify the system capacitance and the electric field distribution. A high dielectric constant packing likely promotes partial discharging between solid beads, hindering homogeneous plasma propagation across a packed bed [21–23]. Modeling has shown a transition in plasma discharge on the beads' surface at increasing dielectric constant from a surface ionization discharge to localized filamentary microdischarge [23–25]. The coaxial DBD reactor runs with several materials of dielectric constant spanning from 5 to 1000 and without any packing (an empty reactor). The particle size distribution (250–425 μm) and the applied voltage of 10 kV were kept fixed.

The C_2H_6 conversion and product yields (Fig. 4) for materials of low and medium dielectric constant, such as SiO_2 (ε∼5), Al_2O_3 (ε∼10), and ZrO_2 (ε∼25), feature higher C_2H_6 conversion than the empty reactor and high dielectric constant packings, as TiO_2 (ε∼100) and $BaTiO_3$ (ε∼1000). The main products remain as above. The dissipated power for the same applied voltage changes with material. A dielectric medium is seemingly beneficial to conversion and product yield up to a threshold, above which, the plasma diffusion throughout the bed is hindered and is localized as microdischarges that do not favor C_2H_6 dissociation. Further support was obtained by visual inspection; in contrast to other materials, $BaTiO_3$ features a dimmer plasma inside the bed leading to low emission intensity. However, all materials show filamentary discharge in their electrical waveforms (Figure S2). A comparison at equal dissipated power results in similar waveforms for all materials (Figure S2), but $BaTiO_3$ requires a higher applied voltage to attain the same power, suggesting hindered discharge propagation.

The product selectivity is invariant of the packing material and strongly correlated to the conversion of C_2H_6 (Fig. 4a), except for non-packed bed and $BaTiO_3$. C_2H_4 is the main product under our conditions. The selectivity of the other species does not vary substantially with material. However, $BaTiO_3$ promotes low C_2H_6 conversion which results in enhanced

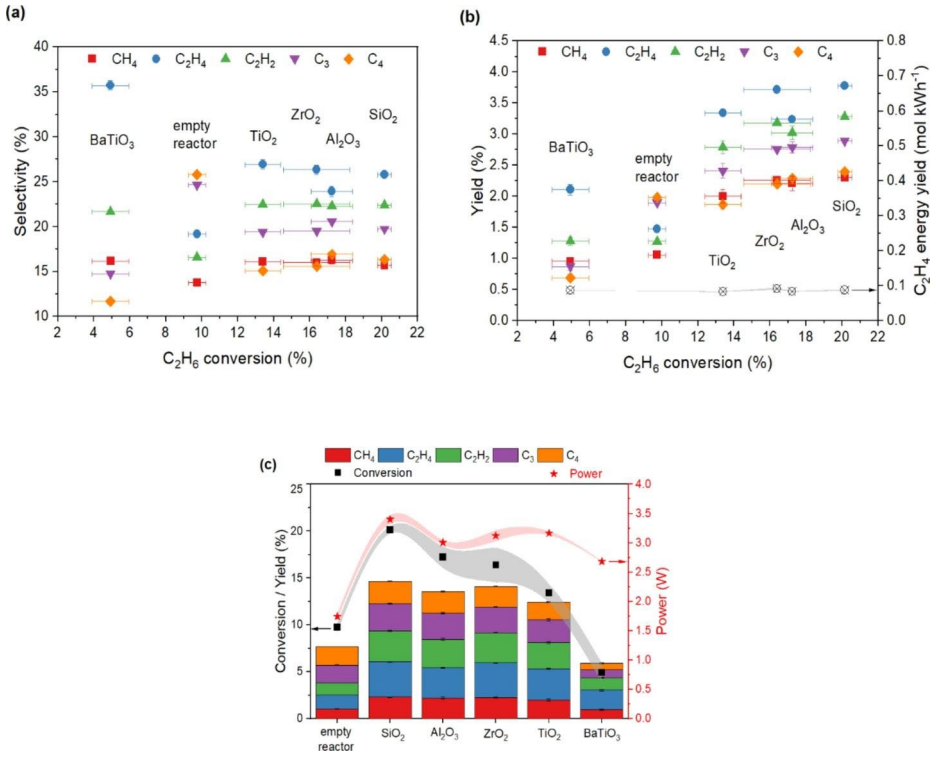

Fig. 4 (a) Product selectivity vs. C_2H_6 conversion for various packings. (b) Product yields and C_2H_4 energy yield vs. C_2H_6 conversion. The X-Y axis error bars refer to the variation of conversion and selectivity/yield across 3 repetitions. (c) Product yields, C_2H_6 conversion, and dissipated power with different dielectric materials in the plasma zone. Shaded curves represent error range. C_2H_6 feed concentration: 5%. Total flow rate: 60 sccm. Applied voltage: 10 kV (peak-to-peak). A higher C_2H_6 conversion relates to higher carbon loss due to more carbon deposit (Table S1)

C_2H_4 selectivity and limited production of recombination products. Conversely, the empty reactor configuration favors generation of C_3 and C_4 species even at intermediate conversion levels (i.e., ~10%). This suggests that microdischarges and surface ionization on the dielectric beads surface promote dehydrogenation over cracking as opposed to gas-phase discharges. While the different dielectric materials have marginal effect on product selectivity, the rising conversion trend attained at decreasing dielectric constant results in the product yield trend of Fig. 4b. SiO_2 enables the highest C_2H_4 yield by allowing more energetic discharges through the bed. Therefore, the C_2H_4 energy yield (defined as moles of C_2H_4 per unit of energy dissipated in the plasma) remains constant throughout the experiments as discharge energy is the main driver of C_2H_4 production. For comparison, our packed bed C_2H_6 dehydrogenation attains 0.09 mol_{C2H4} kWh^{-1}, whereas non-oxidative methane coupling in nanosecond pulsed discharge plasma can reach up to 2.2 mol_{C2H4} kWh^{-1} [26]. Other promising technologies based on methane coupling, such as pulsed compression and microwave reactors, have shown energy yield of 0.88 mol_{C2H4} kWh^{-1} and 0.0012 mol_{C2H4} kWh^{-1}, respectively [27, 28]. Fig. 4c shows that different dielectric materials affect the plasma discharge and consequently the dissipated power. As a result, C_2H_6 conversion fol-

lows the power trend and in turn drives product yield. By increasing the permittivity of the packing bed, discharge power and conversion drop.

As SiO_2 achieves the highest C_2H_4 yield, we further studied the effect of process parameters. The particle size of SiO_2 beads was varied between 145 and 560 µm. The particle size does not play a major role either in the conversion or the product distribution (Fig. 5a) except for a higher conversion attained using smaller particles (i.e., 145–250 µm). The influence of dielectric particles in a plasma environment is not fully discerned; however, modeling studies suggest that the electric field intensifies at the contact point between packing particles, leaving the bed less exposed to an intense electric field [22]. Thus, the smallest beads (i.e., 145–250 µm in Fig. 5a) possess more contact that could enhance localized C_2H_6 dissociation via increased electric field and electron temperature [29]. Increasing conversion at decreasing particle size has also been observed for CO_2 conversion in a DBD plasma reactor [30]. Moreover, the plasma in the packed bed is unstable as a flickering light is seen. This could be due to the pressure increase (from 1.05 to 1.5 atm), resulting from a denser packing that affects the plasma properties. To the contrary, lower residence time is attained with a denser packing, but this phenomenon cannot explain the observed conversion trend.

The gas-bulk temperature is expected to rise at high pressure, but this effect is more relevant in warm plasmas where the H abstraction could dominate the electron-impact dissociation [12]. Nevertheless, the electrical waveforms for different experiments (Figure S3) show the typical filamentary nature of the plasma at all conditions. A slightly lower current

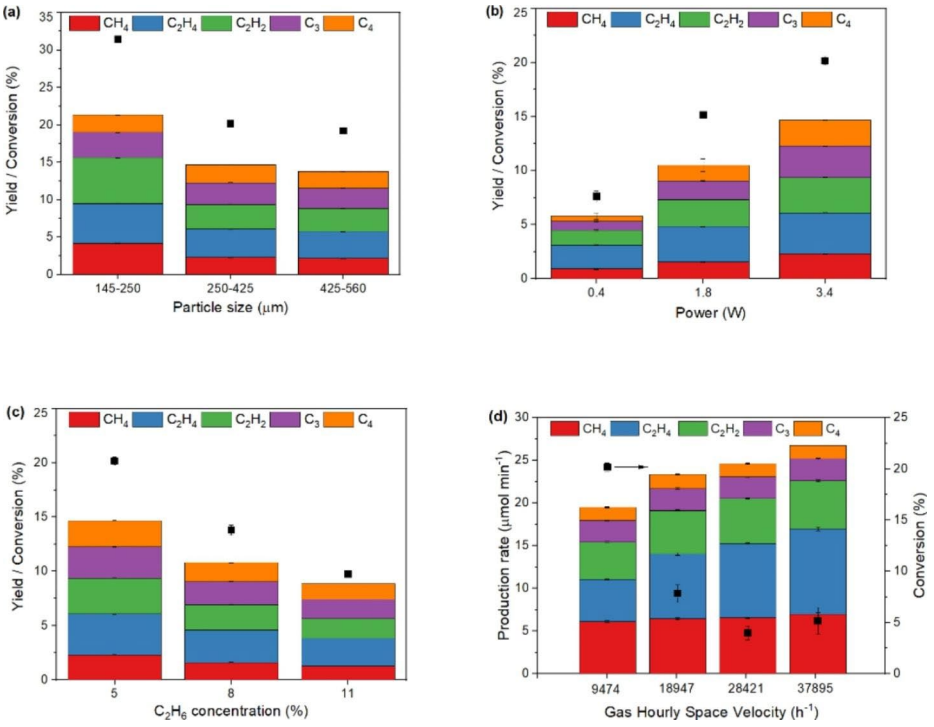

Fig. 5 Products yields and C_2H_6 conversion at varying (a) SiO_2 particle size, (b) dissipated power and (c) initial C_2H_6 concentration. (d) Production rate and C_2H_6 conversion (squares) vs. gas hourly space velocity

observed for the finest particles could possibly be rationalized by the lower reduced electric field at increasing pressure. Therefore, the difference in conversion is more likely caused by the different plasma-surface interactions that result from a denser packing with increasing pressure.

The C_2H_6 conversion and the product yields for different power levels are displayed in Fig. 5b. The C_2H_6 conversion depends linearly on the dissipated power (which in turn is directly proportional to the applied voltage), due to increasing electron density and temperature which promote the electron impact dissociation reactions. The C_2H_4 selectivity decreases upon increasing power, likely due to higher C_2H_4 electron impact dissociation reactions and radical recombination reactions into larger hydrocarbons (Fig. 3), whereas the selectivity to C_2H_2 and CH_4 remains almost constant.

Increasing the C_2H_6 inlet molar fraction at a fixed total gas flow rate (60 sccm) hampers both the He breakdown and the plasma sustainment (Fig. 5c) resulting in lower conversion and higher C_2H_4 selectivity, whereas the ratio CH_4/C_2H_2 and the selectivity of C_3 and C_4 species are seemingly unaffected.

Since the C_2H_4 selectivity drops with increasing C_2H_6 conversion due to extensive electron impact dissociation (Fig. 3), a strategy to enhance the C_2H_4 productivity would be to lower the contact time by increasing the gas flow rate. Figure 5d displays the production rate (calculated as the product concentration times the total gas flow rate) of the main products and C_2H_6 conversion vs. gas space velocity (calculated as total gas flow rate over reactor volume). The higher flow rates are characterized by low C_2H_6 conversions due to the short space times but higher C_2H_4 production rates. The production rates of CH_4 and C_2H_2 also increase with the total gas flow rate but to a lower degree as they are the products of C_2H_4 dissociation. Contrariwise, the production rates of C_3 and C_4 are almost constant.

Despite changing several operating parameters (i.e., packing dielectric constant and particle size, applied power and initial feed concentration), the main products (i.e., CH_4, C_2H_4 and C_2H_2) are correlated to the conversion. Owing to the reaction network proposed in Fig. 3, C_2H_4 and C_2H_2 are mostly generated via electron impact dissociation reactions of C_2H_6 (Eq. 4), according to Eq. 5 and Eq. 6, respectively. No radical species are included in the mass balance as their concentration is not experimentally measured and should be negligible in the product stream compared to the major stable species due to the high reactivity (low lifetime). Their high reactivity results from high rate coefficients that must be accounted for in a more detailed model. The electron density n_e (cm^{-3}) is unknown but it is constant in all equations. Therefore, electron density is embedded in the reaction rate constants for electron impact dissociation of C_2H_6, C_2H_4, and C_2H_2 that are indicated as k_1, k_2, and k_3 (s^{-1}), respectively. Molar flow rates, F of all C_2 species are expressed in mol s^{-1}, whereas species concentrations, C are calculated in mol cm^{-3} and reactor volume, V in cm^{-3}.

$$F_{C_2H_6} - F^0_{C_2H_6} = -k_1 \cdot \mathrm{C_2H_6} \cdot \mathrm{dV} \tag{4}$$

$$F_{C_2H_4} - F^0_{C_2H_4} = 0.46 \cdot k_1 \cdot \mathrm{C_2H_6} \cdot \mathrm{dV} - k_2 \cdot \mathrm{C_2H_4} \cdot \mathrm{dV} \tag{5}$$

$$F_{C_2H_2} - F^0_{C_2H_2} = 0.11 \cdot k_1 \cdot \mathrm{C_2H_6} \cdot \mathrm{dV} + 0.4 \cdot k_2 \cdot \mathrm{C_2H_4} \cdot \mathrm{dV} - k_3 \cdot \mathrm{C_2H_2} \cdot \mathrm{dV} \tag{6}$$

Albeit simplified, this reaction network is consistent with our experimental data. Figure 6a presents all experimental C_2H_4 and C_2H_2 production data for the abovementioned parametric studies at varying C_2H_6 consumption. Both species vary linearly following Eq. 5 and Eq. 6 and the higher slope for the C_2H_4 production than C_2H_2 reflects the higher branching ratio of C_2H_6 dissociation (0.46 vs. 0.11) [19]. These factors are employed to account for the different contributions of the dissociation reaction pathways represented in Fig. 3. Nonetheless, dissociation of C_2H_4 is favored at higher C_2H_6 conversion, resulting in increased production of C_2H_2 (Fig. 6a-b).

Figure 6c reports the reaction rate constants calculated from Eqs. 4–6 based on the experimental dataset of Fig. 4. Both k_1 and k_2 decrease with increasing dielectric constant due to the lower electron density [29] (embedded in the rate constant) attained at lower power (Fig. 4c). The C_2H_4 dissociation rate constant is one order of magnitude higher than that of C_2H_6, thus C_2H_4 is quickly dissociated into C_2H_2 as confirmed by Fig. 6b. The ratio between the two rate constants eliminates the dependence on the electron density. A rather constant ratio is observed, except for high dielectric media (e.g., $BaTiO_3$) that feature lower dissipated power, hence a lower gas temperature (i.e., 50 °C vs. 75 °C for all other materials). k_3 shows a decreasing trend at increasing dielectric constant as well; however, negative values are obtained indicating that C_2H_2 dissociation is negligible and radical recombination to form C_2H_2 (Fig. 3) should not be excluded.

Since the product distribution is driven by the C_2H_6 conversion rather than the materials or process parameters, a catalytic material was tested to assess if a catalyst could alter the gas-phase chemistry at the solid surface. Palladium (Pd) is an effective hydrogenation catalyst and a few examples have been reported for plasma-generated C_2H_2 hydrogenation to C_2H_4 [12, 16]. Therefore, Pd deposited on SiO_2 was tested at varying metal loading (i.e., 0.5, 2, 5 wt%). The metal surface is expected to enhance the electric field and charge redistribution near the metal surface [31, 32] and the radical surface quenching compared to an inert surface [33].

Figure 7a confirms that Pd particles on SiO_2 seemingly distort the applied electric field similarly to high dielectric constant materials (Fig. 4) as the C_2H_6 conversion decreases at increasing catalyst content. The charge redistribution is reflected on the electrical waveforms acquired for the metal loading experiments (Figure S2) where more pronounced current spikes are observed upon increasing catalyst loading. Furthermore, the confinement of plasma discharges on the beads contact points could explain the dimmer plasma observed for the high catalyst loading condition.

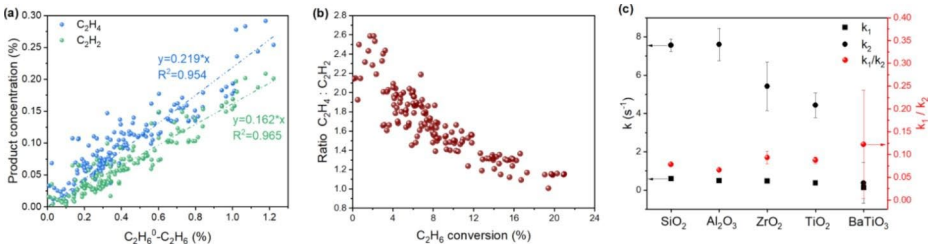

Fig. 6 (a) C_2H_4 (blue spheres) and C_2H_2 (green spheres) production at varying C_2H_6 consumption extent. (b) Ratio between produced C_2H_4 and C_2H_2 vs. C_2H_6 conversion. (c) Reaction rate constants for C_2H_6 and C_2H_4 dissociation and their ratio according to Eqs. 4 and 5

Besides the electric field effect, Pd/SiO_2 modifies the product selectivity (Fig. 7b). The H radicals formed through electron impact dissociation reactions (Fig. 3) are expected to recombine with hydrocarbon radicals on the catalyst surface to generate saturated species. More specifically, C_2H_2 production is almost completely hindered, and instead more CH_4 is attained. Similarly, C_2H_6 formation via complete hydrogenation of C_2H_2 alongside recombination of alkyl and hydrogen radicals could be promoted by Pd, contributing to the lower conversion. The C_2H_4 selectivity is also negatively impacted in favor of CH_4 and saturated C_3-C_4 species. Production of propyne (C_3H_4) is completely prevented whereas the selectivity of butene (C_4H_8) on the 5 wt% Pd/SiO_2 halves compared to bare SiO_2. The observed selectivity shift, where C_2H_2 production is suppressed even with the lowest catalyst loading, proves the catalytic activity of the Pd particles, thus breaking the correlation between C_2H_4/C_2H_2 generation and C_2H_6 consumption observed for all other experimental sets (Fig. 6). Nonetheless, C_2H_4 selectivity must be optimized by tuning the degree of hydrogenation. Low catalyst loading could favor partial C_2H_2 hydrogenation, while low applied power could prevent further dissociation of C_2H_4. The high activity of the Pd catalyst at low temperature could also enable a post-plasma catalytic step where C_2H_2 formed in the plasma discharge converts into C_2H_4 downstream the plasma zone.

A quantification of the hydrogenation effect of the catalyst is possible by comparing all the saturated product species (CH_4 and C_3H_8) with the unsaturated ones (C_2H_4, C_2H_2, C_3H_6, C_3H_4). The C_4 species were not accounted for as their full identification was not possible

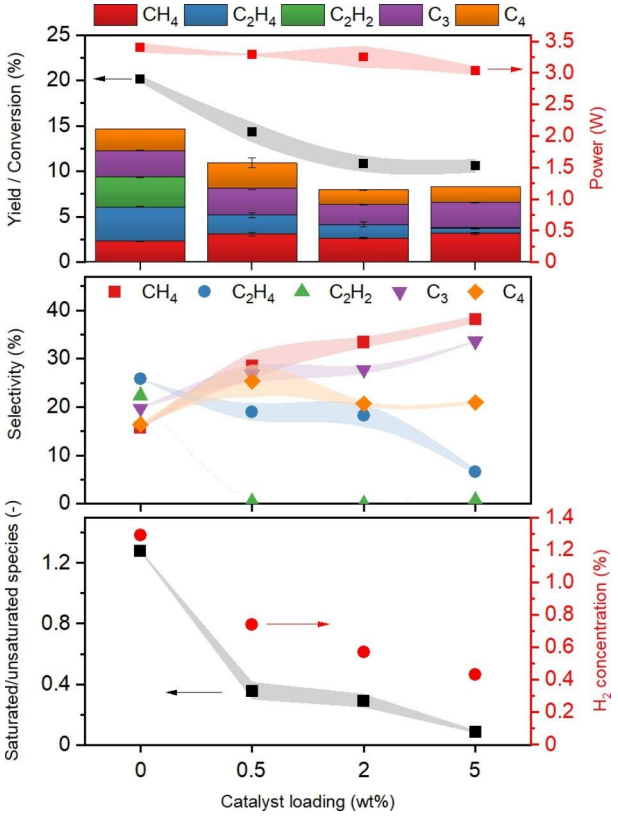

Fig. 7 Effect of Pd catalyst loading on: (a) C_2H_6 conversion, product yield, and dissipated power (b) product selectivity and (c) ratio between unsaturated species (i.e., C_2H_4, C_2H_2, C_3H_6, C_3H_4) and saturated species (i.e., CH_4 and C_3H_8), and H_2 outlet concentration. Shaded areas refer to error range. Particle size: 250–425 µm, flow rate: 60 sccm (5% C_2H_6 in He), applied voltage: 10 kV (peak-to-peak)

due to their large number. The effective utilization of the produced H_2 by the catalyst to drive hydrogenation, clearly observed in Fig. 7c through the decreasing trend of the ratio between unsaturated and saturated species, mirrors the outlet H_2 concentration for the different catalyst loadings.

Furthermore, by promoting hydrogenation, C_2H_2 oligomerization and ultimately carbon deposit are hindered, as observed for Pd-catalyzed CH_4 coupling [11]. Thus, a higher carbon balance is attained at higher catalyst loading (Table S1).

The plasma-assisted activation of C_2H_6 overcomes thermodynamic limitations as the equilibrium conversion of EDH at the operating temperature (i.e., max 70 °C) is $2*10^{-5}$% vs. the observed one of 20%. The thermocatalytic EDH operates above 600 °C giving C_2H_4 selectivity > 90% at C_2H_6 conversion below 50% [5, 34, 35]. The energy demand of these processes compared to the industrial state of the art steam cracking is not currently available. The latter requires 17–21 GJ t_{C2H4}^{-1} including process energy for separation [36]. The energy demand of the non-optimized plasma reactor is much higher than the industrial benchmark (about 50 times). The ODH plasma processes consume ~ 2.5 and 10X more energy than our reactor, with the exception of the Pd catalyzed ODH that requires about 45% less specific energy input [16–18]. Nonetheless, the fully electric process could compete with thermal cracking in terms of carbon footprint. Life Cycle Assessment (LCA) of C_2H_4 production through plasma-driven CH_4 coupling shows that a plasma process powered by renewable wind energy generates CO_2 emissions lower than shale gas thermal cracking and comparable to naphtha steam cracking [37].

Conclusions

We explored the non-oxidative upgrading of C_2H_6 in a coaxial packed-bed DBD plasma reactor to produce light hydrocarbons by varying operational parameters, such as packing material and particle size, dissipated power, C_2H_6 inlet concentration, and flow rate. The main product is C_2H_4 followed by C_2H_2 and then CH_4 and C_3/C_4 hydrocarbons. The chemistry is clearly dominated by electron impact dissociation and radical recombination reactions. Packing materials of varying dielectric properties (i.e., SiO_2, Al_2O_3, ZrO_2, TiO_2, and $BaTiO_3$) alter the electric field distribution and the dissipated power, hence directly governing C_2H_6 conversion which drops almost four-fold with increasing dielectric constant. Nonetheless, the C_2H_4 energy yield remains constant across materials. The most abundant product selectivity (C_2H_4, C_2H_2 and CH_4) correlates linearly with the C_2H_6 conversion. The introduction of a Pd catalyst on the SiO_2 support distorts the electric field and alters the product selectivity. Hydrogenation produces more saturated species by consuming H_2. The H_2 concentration is almost 3 times lower over 5 wt% Pd/SiO_2 catalyst than bare SiO_2.

Supplementary Information The online version contains supplementary material available at https://doi.org/10.1007/s11090-023-10343-w.

Acknowledgements This work was supported from Department of Energy's Office of Energy Efficient and Renewable Energy's Advanced Manufacturing Office under Award Number DE-EE0007888-8.3. The Delaware Energy Institute gratefully acknowledges the support and partnership of the State of Delaware toward the RAPID projects.

Author Contribution F.C. Conceptualization, Investigation, Writing - Original Draft. P.D. Conceptualization, Writing - Review & Editing. G.D.S. Conceptualization, Writing - Review & Editing. D.G.V. Conceptualization, Writing - Review & Editing.

Funding This work has received funds from the U.S. Department of Energy, DE-EE0007888-8.3.

Data Availability All data generated during this study is reported in the article and the supplementary material.

Declarations

Ethical Approval Not applicable.

Competing Interests The authors declare no competing interests.

References

1. Porosoff MD, Myint MNZ, Kattel S, Xie Z, Gomez E, Liu P, Chen JG (2015) Identifying different types of catalysts for CO2 reduction by ethane through dry reforming and oxidative dehydrogenation, Angew. Chemie - Int Ed 54:15501–15505. https://doi.org/10.1002/anie.201508128
2. Kim S, Oh S (2020) Impact of US Shale Gas on the Vertical and Horizontal Dynamics of Ethylene Price. Energies 13. https://doi.org/10.3390/EN13174479
3. Dai Y, Gao X, Wang Q, Wan X, Zhou C, Yang Y (2021) Recent progress in heterogeneous metal and metal oxide catalysts for direct dehydrogenation of ethane and propane. Chem Soc Rev 50:5590–5630. https://doi.org/10.1039/d0cs01260b
4. Wang C, Yang B, Gu Q, Han Y, Tian M, Su Y, Pan X, Kang Y, Huang C, Liu H, Liu X, Li L, Wang X (2021) Near 100% ethene selectivity achieved by tailoring dual active sites to isolate dehydrogenation and oxidation. Nat Commun 12:1–8. https://doi.org/10.1038/s41467-021-25782-2
5. Wu L, Fu Z, Ren Z, Wei J, Gao X, Tan L, Tang Y (2021) Enhanced Catalytic Performance of Fe-containing HZSM-5 for ethane non-oxidative dehydrogenation via Hydrothermal Post-Treatment, ChemCatChem. 13 4019–4028. https://doi.org/10.1002/cctc.202100752
6. Bogaerts A, Neyts EC (2018) Plasma technology: an Emerging Technology for Energy Storage. ACS Energy Lett 3:1013–1027. https://doi.org/10.1021/acsenergylett.8b00184
7. Mehta P, Barboun P, Go DB, Hicks JC, Schneider WF (2019) Catalysis enabled by plasma activation of strong Chemical Bonds: a review. ACS Energy Lett 4:1115–1133. https://doi.org/10.1021/acsenergylett.9b00263
8. Scapinello M, Delikonstantis E, Stefanidis GD (2017) The panorama of plasma-assisted non-oxidative methane reforming. Chem Eng Process Process Intensif 117:120–140. https://doi.org/10.1016/j.cep.2017.03.024
9. Abiev RS, Sladkovskiy DA, Semikin KV, Murzin DY, Rebrov EV (2020) Non-thermal plasma for process and energy intensification in dry reforming of methane. Catalysts 10:1–41. https://doi.org/10.3390/catal10111358
10. Kameshima S, Mizukami R, Yamazaki T, Prananto LA, Nozaki T (2018) Interfacial reactions between DBD and porous catalyst in dry methane reforming. J Phys D Appl Phys 51. https://doi.org/10.1088/1361-6463/aaad7d

11. García-Moncada N, van Rooij G, Cents T, Lefferts L (2021) Catalyst-assisted DBD plasma for coupling of methane: minimizing carbon-deposits by structured reactors. Catal Today 369:210–220. https://doi.org/10.1016/J.CATTOD.2020.04.028
12. Delikonstantis E, Scapinello M, Van Geenhoven O, Stefanidis GD (2020) Nanosecond pulsed discharge-driven non-oxidative methane coupling in a plate-to-plate electrode configuration plasma reactor. Chem Eng J 380:122477. https://doi.org/10.1016/j.cej.2019.122477
13. Jensen RJ, Bell AT, Soong DS (1983) Plasma polymerization of ethane. I. Experimental studies of effluent gas composition and polymer deposition rates. Plasma Chem Plasma Process 3:139–161. https://doi.org/10.1007/BF00566018
14. Jensen RJ, Bell AT, Soong DS (1983) Plasma polymerization of ethane. II. Theoretical analysis of effluent gas composition and polymer deposition rates. Plasma Chem Plasma Process 3:163–192. https://doi.org/10.1007/BF00566019
15. Sanchez-Gonzalez R, Kim Y, Rosocha LA, Abbate S (2007) Methane and ethane decomposition in an atmospheric-pressure plasma jet. IEEE Trans Plasma Sci 35:1669–1676. https://doi.org/10.1109/TPS.2007.910743
16. Zhang X, Zhu A, Li X, Gong W (2004) Oxidative dehydrogenation of ethane with CO2 over catalyst under pulse corona plasma. Catal Today 89:97–102. https://doi.org/10.1016/j.cattod.2003.11.015
17. Trionfetti C, Ağıral A, Gardeniers HJGE, Lefferts L, Seshan K (2008) Alkane activation at ambient temperatures: unusual selectivities, C-C, C-H bond scission versus C-C bond coupling, ChemPhysChem. 9 533–537. https://doi.org/10.1002/cphc.200700757
18. Biswas AN, Winter LR, Loenders B, Xie Z, Bogaerts A, Chen JG (2022) Oxygenate production from plasma-activated reaction of CO2and ethane. ACS Energy Lett 7:236–241. https://doi.org/10.1021/acsenergylett.1c02355
19. Janev RK, Reiter D (2004) Collision processes of C2,3Hy and C 2,3Hy + hydrocarbons with electrons and protons. Phys Plasmas 11:780–829. https://doi.org/10.1063/1.1630794
20. Heijkers S, Aghaei M, Bogaerts A, Plasma-Based CH (2020) 4 Conversion into Higher Hydrocarbons and H2: modeling to reveal the reaction mechanisms of different plasma sources. J Phys Chem C 124:7016–7030. https://doi.org/10.1021/acs.jpcc.0c00082
21. Taheraslani M, Gardeniers H (2020) Coupling of CH4 to C2 hydrocarbons in a packed bed DBD plasma reactor: the effect of dielectric constant and porosity of the packing. Energies 13. https://doi.org/10.3390/en13020468
22. Wang W, Kim HH, Van Laer K, Bogaerts A (2018) Streamer propagation in a packed bed plasma reactor for plasma catalysis applications. Chem Eng J 334:2467–2479. https://doi.org/10.1016/j.cej.2017.11.139
23. Wang W, Butterworth T, Bogaerts A (2021) Plasma propagation in a single bead DBD reactor at different dielectric constants: insights from fluid modelling. J Phys D Appl Phys 54. https://doi.org/10.1088/1361-6463/abe8ff
24. Bogaerts A, Zhang QZ, Zhang YR, Van Laer K, Wang W (2019) Burning questions of plasma catalysis: answers by modeling. Catal Today 337:3–14. https://doi.org/10.1016/j.cattod.2019.04.077
25. Engeling KW, Kruszelnicki J, Kushner MJ, Foster JE (2018) Time-resolved evolution of micro-discharges, surface ionization waves and plasma propagation in a two-dimensional packed bed reactor. Plasma Sources Sci Technol 27. https://doi.org/10.1088/1361-6595/aad2c5
26. Delikonstantis E, Scapinello M, Stefanidis GD (2018) Low energy cost conversion of methane to ethylene in a hybrid plasma-catalytic reactor system. Fuel Process Technol 176:33–42. https://doi.org/10.1016/j.fuproc.2018.03.011
27. Slotboom Y, Roosjen S, Kronberg A, Glushenkov M, Kersten SRA (2021) Methane to ethylene by pulsed compression. Chem Eng J 414. https://doi.org/10.1016/j.cej.2021.128821
28. Julian I, Ramirez H, Hueso JL, Mallada R, Santamaria J (2019) Non-oxidative methane conversion in microwave-assisted structured reactors. Chem Eng J 377. https://doi.org/10.1016/j.cej.2018.08.150
29. Van Laer K, Bogaerts A (2017) How bead size and dielectric constant affect the plasma behaviour in a packed bed plasma reactor: a modelling study. Plasma Sources Sci Technol 26(8):085007
30. Uytdenhouwen Y, Van Alphen S, Michielsen I, Meynen V, Cool P, Bogaerts A (2018) A packed-bed DBD micro plasma reactor for CO2 dissociation: does size matter? Chem Eng J 348:557–568
31. Kruszelnicki J, Engeling KW, Foster JE, Kushner MJ (2021) Interactions between atmospheric pressure plasmas and metallic catalyst particles in packed bed reactors. J Phys D Appl Phys 54. https://doi.org/10.1088/1361-6463/abcc92
32. Jo S, Kim T, Lee DH, Kang WS, Song YH (2014) Effect of the electric conductivity of a catalyst on methane activation in a dielectric barrier discharge reactor. Plasma Chem Plasma Process 34:175–186. https://doi.org/10.1007/s11090-013-9505-1

33. Aghalayam P, Bui PA, Vlachos DG (1998) The role of radical wall quenching in flame stability and wall heat flux: hydrogen-air mixtures. Combust Theory Model 2:515–530. https://doi.org/10.1088/1364-7830/2/4/010
34. Pan Y, Bhowmick A, Wu W, Zhang Y, Diao Y, Zheng A, Zhang C, Xie R, Liu Z, Meng J, Liu D (2021) Titanium Silicalite-1 Nanosheet-Supported platinum for non-oxidative ethane dehydrogenation. ACS Catal 11:9970–9985. https://doi.org/10.1021/acscatal.1c02676
35. De S, Ould-Chikh S, Aguilar A, Hazemann JL, Zitolo A, Ramirez A, Telalovic S, Gascon J (2021) Stable Cr-MFI catalysts for the nonoxidative dehydrogenation of ethane: Catalytic Performance and Nature of the active Sites. ACS Catal 11:3988–3995. https://doi.org/10.1021/acscatal.0c05170
36. Ren T, Patel M, Blok K (2006) Olefins from conventional and heavy feedstocks: Energy use in steam cracking and alternative processes. Energy 31:425–451. https://doi.org/10.1016/j.energy.2005.04.001
37. Delikonstantis E, Igos E, Augustinus M, Benetto E, Stefanidis GD (2020) Life cycle assessment of plasma-assisted ethylene production from rich-in-methane gas streams. Sustain Energy Fuels 4:1351–1362